

Zero-bias crossings and peculiar Shapiro maps in graphene Josephson junctions

T. F. Q. Larson,¹ L. Zhao,¹ E. G. Arnault,¹ M. T. Wei,¹ A. Seredinski,¹
H. Li,² K. Watanabe,³ T. Taniguchi,³ F. Amet,² and G. Finkelstein¹

¹*Department of Physics, Duke University, Durham, NC 27708, USA.*

²*Department of Physics and Astronomy, Appalachian State University, Boone, NC 28607, USA.*

³*Advanced Materials Laboratory, National Institute for Materials Science, 1-1 Namiki, Tsukuba, 305-0044, Japan.*

(Dated: February 2, 2022)

The AC Josephson effect manifests itself in the form of “Shapiro steps” of quantized voltage in Josephson junctions subject to RF radiation. This effect presents an early example of a driven-dissipative quantum phenomenon and is presently utilized in primary voltage standards. Shapiro steps have also become one of the standard tools to probe junctions made in a variety of novel materials. Here, we study Shapiro steps in a widely tunable graphene-based Josephson junction. We investigate the variety of patterns that can be obtained in this well-understood system depending on the carrier density, temperature, RF frequency, and magnetic field. Although the patterns of Shapiro steps can change drastically when just one parameter is varied, the overall trends can be understood and the behaviors straightforwardly simulated. The resulting understanding may help in interpreting similar measurements in more complex materials.

Josephson junctions subject to an external RF radiation demonstrate the inverse AC Josephson effect: the phase difference across the junction locks to the external frequency [1]. As a result, the phase steadily ramps with time, and the $I - V$ curves form “Shapiro steps” of quantized voltage $V = n\hbar\omega/2e$, where n counts the number of 2π periods by which the phase progressed over one period of excitation [2]. The exact mechanisms of the phase locking and its stability were investigated in detail in the 1980s [3]. The extremely precise voltage quantization of the steps is presently utilized in primary voltage standards [4].

Recently, interest in topological Josephson junctions have reinvigorated the use of the AC Josephson effect as a tool to probe a junction’s current-phase relation (CPR) [5, 6]. Missing steps and residual supercurrent associated with the anomalous CPR are some of the signatures which have been explored [7–11]. Many of these studies are performed at relatively low power and frequency; in this regime the measured maps are significantly different from the textbook “Bessel function” patterns even in topologically trivial junctions [3]. In this paper, we study the inverse Josephson effect in graphene-based superconductor-normal-superconductor (SNS) junctions. Shapiro steps in this topologically trivial material have been previously explored [12–15] and used as a reference in the study of topological junctions [16]. We show that a variety of patterns can be obtained within the same junction by tuning the gate voltage and magnetic field. Both the Bessel function regime and the strongly hysteretic regime with “zero bias crossings” are observed. We directly simulate the observed patterns using an extension of the resistively and capacitively shunted junction (RCSJ) model and qualitatively explain the observed trends.

Our sample is made of exfoliated graphene encapsulated in hexagonal boron nitride [17]. The superconducting leads are made by sputtering molybdenum-rhenium alloy [18], which has a relatively large gap of 1.3 meV. The sample is measured in a dilution refrigerator with

the sample holder temperature of approximately 100 mK, which depends weakly on the applied RF signal. The actual sample temperature under the RF drive could be higher [19]. The GHz drive is coupled by an antenna placed approximately 1 mm away from the sample. The exact value of the RF power reaching the sample is difficult to quantify because of the frequency-dependent coupling between the antenna and the sample, which are not impedance matched. We therefore only list the nominal RF power emitted by the generator at room temperature, which is a common practice in similar experiments. To measure the DC voltage across the sample, we perform multiple DC current bias sweeps while keeping the rest of the parameters fixed. The resulting $I - V$ curves are then averaged and numerically differentiated to obtain the differential resistance $R = dV/dI$.

We start by comparing patterns of Shapiro steps at frequencies of 3 and 5 GHz and several values of magnetic field applied perpendicular to the junction (Figure 1). Magnetic field allows us to conveniently vary the critical current I_C without changing other junction parameters. The maps in Figure 1 present the differential resistance R ; the dark regions correspond to the steps of constant voltage, and the narrow bright lines correspond to the transitions between these steps. The current bias is swept from negative to positive, resulting in pronounced hysteresis in some of the features. For example, at low applied power, the central dark region corresponding to supercurrent appears asymmetric, with the switching current at positive bias being significantly larger than the retrapping current at negative bias. Many of the step transitions show hysteresis as well.

Following Ref. [3], we introduce a convenient dimensionless parameter, $\Omega = \omega/\omega_p$, which is crucial in determining the pattern of Shapiro steps. (Here, ω is the RF drive frequency and $\omega_p = \sqrt{2eI_C/\hbar C}$ is the plasma frequency of the junction.) Ω grows left to right and bottom to top in Figure 1. Shapiro patterns measured at different ω and I_C but comparable Ω , (see the three pairs (a and f), (b and g), and (c and h) in Figure 1) demonstrate

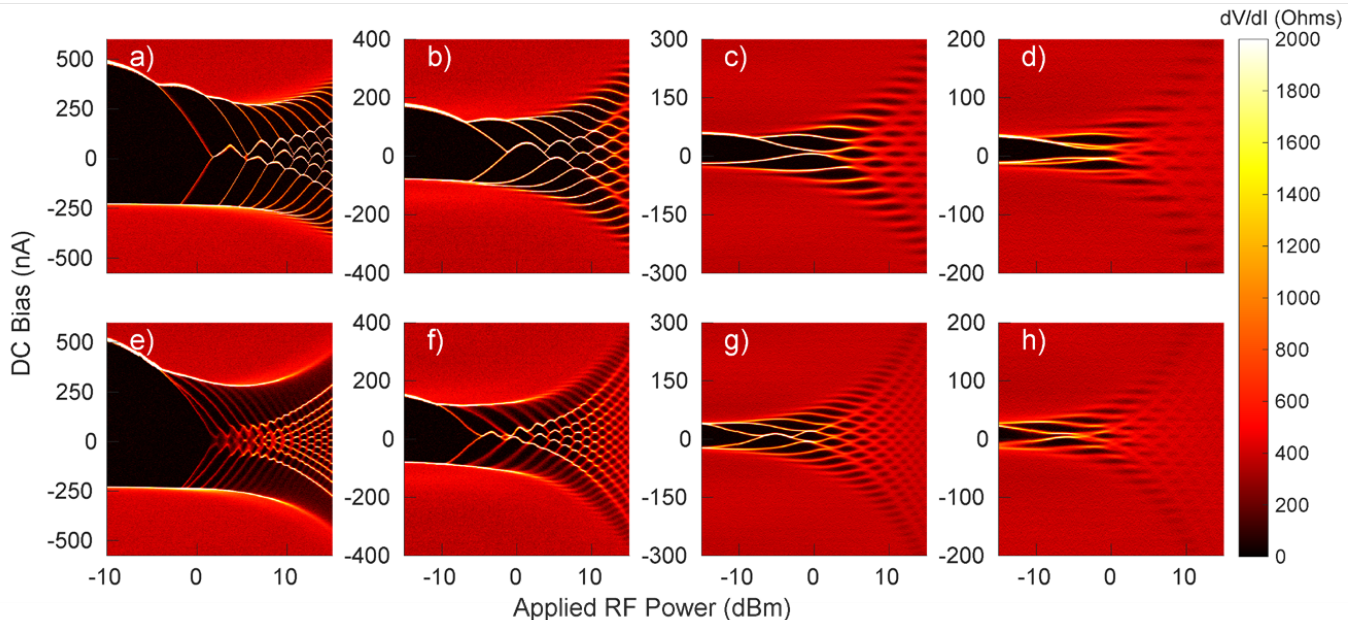


FIG. 1. The maps of differential resistance showing Shapiro steps as a function of the DC bias current, I , and RF power, P_{RF} . The gate voltage for this figure through Figure 4 is set at $V_G = +0.45$ V as measured from the Dirac peak ($V_D = -10$ mV is negligible in this sample). The maps are measured at two frequencies (top row: 5 GHz, bottom row: 3 GHz) and different critical currents (left to right: $I_S = 650, 240, 80$ and 35 nA), as tuned by perpendicular magnetic field). An important dimensional parameter controlling the overall behavior is $\Omega = \omega/\omega_p \propto \omega/\sqrt{I_C}$. The pairs of panels (a and f), (b and g), (c and h) correspond to roughly equal values of Ω and therefore appear similar. We observe the expected trends, according to which at high Ω (right panels) the plateaus are centered at fixed voltages and their vertical extent is described by the Bessel functions. In the opposite limit of low Ω (left panels), many features of the maps become hysteretic, and the $n \neq 0$ plateaus cross zero bias.

qualitative similarity.

For the smallest I_C (highest Ω , Figures 1c, d, and h), the pattern of Shapiro steps follows the Bessel function dependence [20]. In this regime, the extent of the steps in the bias direction is roughly proportional to the Bessel function $J_n(i)$, where $i = I_{RF}/I_C$ is the ratio of the applied RF current to the critical current [21]. The steps are centered at $I = V_n/R_j$, where R_j is the effective DC shunt resistance of the junction. Experimentally, we can extract the effective value of the shunt resistance, $R_j \approx 250$ Ohms, independent of I_C through Figure 1. Note that this value is comparable, but slightly smaller than the normal resistance of the junction $R_N \approx 450$ Ohms [20].

As the critical current increases on the left panels of Figure 1, the patterns change due to the coexistence of multiple stable steps for a given bias value [15]. The plateaus are no longer centered around a fixed current bias of V_n/R_j , but instead emerge sequentially from the normal state boundary and diagonally descend toward zero bias. At high RF power multiple step boundaries intersect, resulting in an intricate net of transitions (Figures 1a, b, f and g). Finally, for the lowest Ω (Figure 1e), the ± 1 steps no longer reach zero upon the first approach, and the $I - V$ curves show a pronounced region of non-quantized voltage close to zero bias (P_{RF} between 0 and 3 dBm).

We now concentrate on the parameters of Figure 1a which is reproduced in Figure 2a. Figure 2c shows a line cut extracted from Figure 2a (blue), as well as a similar line measured for the opposite sweep direction (red). This confirms that the asymmetric features seen in Figure 1 are indeed due to hysteresis, and that for many parameter values multiple solutions are simultaneously stable. Figure 2b is taken under the same conditions, but at a higher temperature ($T=1.5$ K). At this temperature, the hysteresis of the Shapiro features is nearly gone, and a regular pattern emerges, resembling a distorted honeycomb.

Figures 3a,b show numerical simulations which reproduce most of the features in Figures 2a,b. The simulations use the current-biased model of Ref. [21] appropriately modified to account for the capacitance and resistance of the connected pads and leads. Similar to the measurement, time evolution starts at negative bias. We then numerically evolve the equation and average the voltage once the initial transients settle. The final values of ϕ and $\frac{d\phi}{dt}$ are then used as initial conditions for the next bias point. Finally, the sweeps are repeated multiple times and averaged, as is done in the experiment (supplementary material).

These simulations allow us to trace the time evolution of the phase within each cell of the Shapiro map. The examples of the $\phi(t)$ are shown in Figure 3c for several

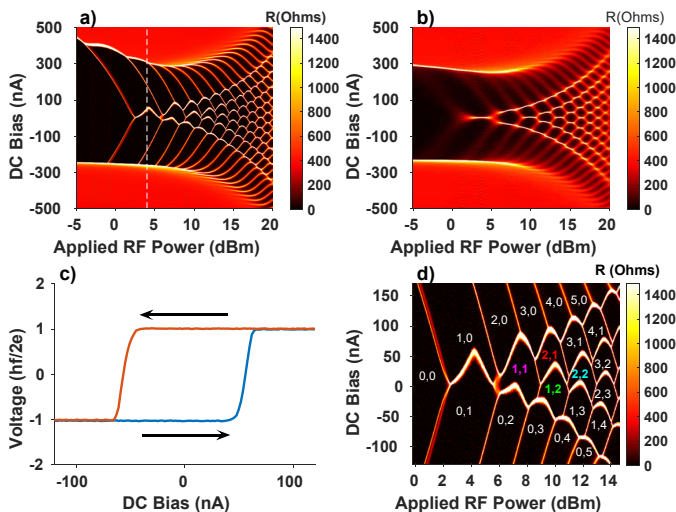


FIG. 2. a) Differential resistance as a function of I and P_{RF} reproducing Figure 1a ($f = 5$ GHz, $I_S = 650$ nA, sample holder temperature $T = 100$ mK). b) A map identical to (a) but measured at $T = 1.5$ K, at which point the hysteresis is largely suppressed. c) A cut through the map (a) taken at $P_{RF} = 4$ dBm (at the dashed line), which shows the hysteretic switching between the $n = 1$ and $n = -1$ steps depending on the sweep direction. d) A zoom of map (a), with the different plateaus labeled by (p, q) as described in the text.

neighboring cells. By analyzing these traces, a rather simple qualitative picture emerges, represented schematically in Figure 3d: For each cycle of RF excitation, the phase progresses over p minima of the washboard potential and then retraces q of them backward. The overall change of phase is $2\pi(p - q)$, and the index of the resulting Shapiro step is $n = p - q$. This behavior has been previously identified in the Bessel function regime [3, 22]. In Figure 2d, we zoom in on the data of Figure 2a and label select cells by their (p, q) indexes. Note that in the resulting regular pattern, each cell in the central part of the map has 6 neighbors. The two neighbors in the vertical direction have the same total number $p + q$ while n differs by 2. The four neighbors on the left/right have either p or q decreased/increased by 1.

Finally, we look at the gate voltage dependence of the maps in Figure 4. While gate voltage influences many parameters, the most significant effect is on I_C and R_j , the latter decreasing by about a factor of roughly 4 between Figures 4a and 4d. We find that near the Dirac peak the hysteresis is very large (Figure 4a), while further away from the Dirac peak the hysteresis of the transitions between the plateaus is significantly suppressed (Figure 4d). This suppression is partially explained by increased damping, rather than the purely thermal smearing as observed in Figure 2b. However, in order to reproduce the data measured at larger gate voltage, we find that it is also necessary to increase the simulated noise level. We straightforwardly increase the simulated current noise level $\propto \frac{1}{\sqrt{R_j}}$, which describes the thermal noise of R_j . The resulting maps are reasonably consistent with the

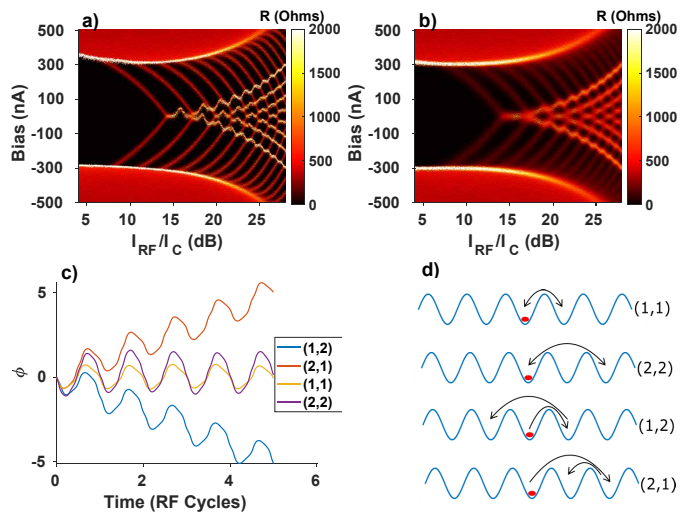


FIG. 3. a,b) Simulation of dV/dI for different noise levels, to be compared to $R_L = 50$ Ohms, $R_j = 300$ Ohms, $I_C = 600$ nA, $C_0 = 2.5$ pF and $f = 5$ GHz. To reproduce the experiment, the simulation starts at the lowest DC bias, averages over 500 RF cycles, and then uses the final values of ϕ and $\frac{d\phi}{dt}$ as the initial conditions for the next value of bias. Ten bias sweeps are produced in this manner and then averaged to reduce noise. c) Numerical traces of $\phi(t)$ on various plateaus labeled by the pairs of (p, q) (see text). d) Schematic of the washboard potential and the four types of phase evolution corresponding to (c). The top two schematics represent different forms of $n = 0$, while the bottom two both show $n = \pm 1$.

experiment (supplemental Figure S3). Noise processes in ballistic SNS junctions require further study in both the equilibrium case and under RF drive.

In conclusion, we have studied the AC Josephson ef-

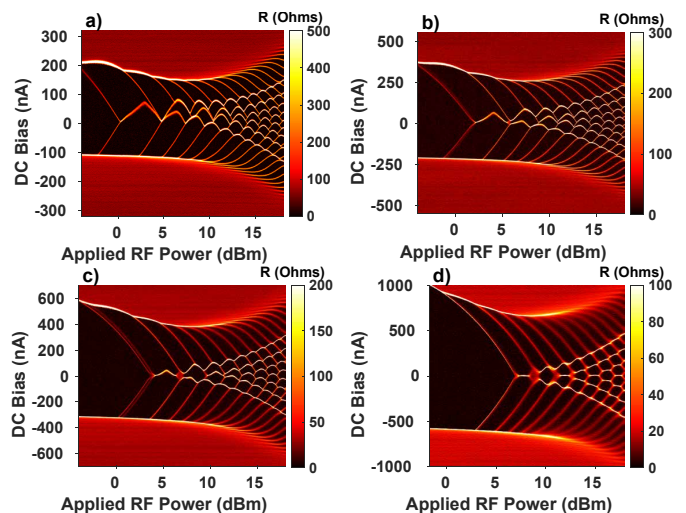


FIG. 4. a-d) Shapiro maps for gate voltages of 0, 0.375, 0.75 and 1.125 V, respectively. Near the Dirac peak, the hysteresis is the most pronounced, with a gradual decline in hysteresis at higher gate voltages. The higher doping both lowers the junction resistance R_j (resulting in higher dissipation) and increases the critical current.

fect in a non-topological graphene junction, which allows one to directly tune many of the relevant parameters. The type of samples studied here provides a highly tunable platform to probe the unexplored aspects of driven-dissipative dynamics of a quantum system. Understanding the variety of Shapiro patterns obtained in a prototypical graphene SNS junction will help to identify the non-trivial features in junctions made of topological materials [7–10]. It also opens interesting perspectives for studying multi-terminal junctions [23–25], which could reveal topological bands when subject to RF drive [26]. Finally, since the Hamiltonian of the RF-driven junction is periodic in the phase difference and in time, it could be considered in the context of Floquet physics, which could potentially result in topologically non-trivial bands (see e.g. Ref. [27]).

ACKNOWLEDGMENTS

We thank M. Dykman, S. Teitsworth and J. Williams for helpful discussions. Low-temperature electronic mea-

surements performed by T.F.L and E.G.A, as well as simulations performed by L.Z., were supported by the Office of Basic Energy Sciences, U.S. Department of Energy, under Award DE-SC0002765. Lithographic fabrication and characterization of the samples performed by M.T.W. and A.S. were supported by ARO Award W911NF16-1- 0122. H. Li, and F.A. acknowledge the ARO under Award W911NF-16-1-0132. K.W. and T.T. acknowledge the Elemental Strategy Initiative conducted by the MEXT, Japan and the CREST (JPMJCR15F3), JST. S.T. and M. Y. acknowledges KAKENHI (GrantNo. 38000131, 17H01138). This work was performed in part at the Duke University Shared Materials Instrumentation Facility (SMIF), a member of the North Carolina Research Triangle Nanotechnology Network (RTNN), which is supported by the National Science Foundation (Grant ECCS-1542015) as part of the National Nanotechnology Coordinated Infrastructure (NNCI).

-
- [1] B. D. Josephson, *Reviews of Modern Physics* **36**, 216 (1964), ISSN 0034-6861.
- [2] S. Shapiro, *Physical Review Letters* **11**, 80 (1963), ISSN 0031-9007.
- [3] R. L. Kautz, *Reports on Progress in Physics* **59**, 935 (1996), ISSN 0034-4885, 1361-6633.
- [4] C. A. Hamilton, *Review of Scientific Instruments* **71** (2000).
- [5] H.-J. Kwon, V. M. Yakovenko, and K. Sengupta, *Low Temperature Physics* **30**, 613 (2004), ISSN 1063-777X, 1090-6517.
- [6] L. Fu and C. L. Kane, *Physical Review B* **79**, 161408 (2009), ISSN 1098-0121, 1550-235X.
- [7] L. P. Rokhinson, X. Liu, and J. K. Furdyna, *Nature Physics* **8**, 795 (2012), ISSN 1745-2473, 1745-2481.
- [8] J. Wiedenmann, E. Bocquillon, R. S. Deacon, S. Hartinger, O. Herrmann, T. M. Klapwijk, L. Maier, C. Ames, C. Brüne, C. Gould, et al., *Nature Communications* **7** (2016), ISSN 2041-1723.
- [9] E. Bocquillon, R. S. Deacon, J. Wiedenmann, P. Leubner, T. M. Klapwijk, C. Brüne, K. Ishibashi, H. Buhmann, and L. W. Molenkamp, *Nature Nanotechnology* **12**, 137 (2017), ISSN 1748-3387, 1748-3395.
- [10] C. Li, J. C. de Boer, B. de Ronde, S. V. Ramankutty, E. van Heumen, Y. Huang, A. de Visser, A. A. Golubov, M. S. Golden, and A. Brinkman, *Nature Materials* **17**, 875 (2018), ISSN 1476-1122, 1476-4660.
- [11] K. Le Calvez, L. Veyrat, F. Gay, P. Plaindoux, C. B. Winkelmann, H. Courtois, and B. Sacépé, *Communications Physics* **2** (2019), ISSN 2399-3650.
- [12] H. B. Heersche, P. Jarillo-Herrero, J. B. Oostinga, L. M. K. Vandersypen, and A. F. Morpurgo, *Nature* **446**, 56 (2007), ISSN 0028-0836, 1476-4687.
- [13] K. Komatsu, C. Li, S. Autier-Laurent, H. Bouchiat, and S. Guéron, *Physical Review B* **86**, 115412 (2012), ISSN 1098-0121, 1550-235X.
- [14] G.-H. Lee, S. Kim, S.-H. Jhi, and H.-J. Lee, *Nature Communications* **6**, 6181 (2015), ISSN 2041-1723.
- [15] S. S. Kalantre, F. Yu, M. T. Wei, K. Watanabe, T. Taniguchi, M. Hernandez-Rivera, F. Amet, and J. R. Williams, arXiv arXiv:1910.10125 (2019), 1910.10125.
- [16] See supplemental of Ref.[8].
- [17] C. R. Dean, A. F. Young, I. Meric, C. Lee, L. Wang, S. Sorgenfrei, K. Watanabe, T. Taniguchi, P. Kim, K. L. Shepard, et al., *Nature Nanotechnology* **5**, 722 (2010), ISSN 1748-3387, 1748-3395.
- [18] V. E. Calado, S. Goswami, G. Nanda, M. Diez, A. R. Akhmerov, K. Watanabe, T. Taniguchi, T. M. Klapwijk, and L. M. K. Vandersypen, *Nature Nanotechnology* **10**, 761 (2015), ISSN 1748-3387, 1748-3395.
- [19] A. De Cecco, K. Le Calvez, B. Sacépé, C. B. Winkelmann, and H. Courtois, *Physical Review B* **93** (2016), ISSN 2469-9950, 2469-9969.
- [20] M. Tinkham, *Introduction to Superconductivity* (Dover, 1996), 2nd ed.
- [21] P. Russer, *Journal of Applied Physics* **43**, 2008 (1972), ISSN 0021-8979, 1089-7550.
- [22] R. E. Thorne, W. G. Lyons, J. W. Lyding, J. R. Tucker, and J. Bardeen, *Physical Review B* **35**, 6360 (1987), ISSN 0163-1829.
- [23] E. Strambini, S. D’Ambrosio, F. Vischi, F. S. Bergeret, Y. V. Nazarov, and F. Giazotto, *Nature Nanotechnology* **11**, 1055 (2016), ISSN 1748-3387, 1748-3395.
- [24] A. W. Draelos, M.-T. Wei, A. Seredinski, H. Li, Y. Mehta, K. Watanabe, T. Taniguchi, I. V. Borzenets, F. Amet, and G. Finkelstein, *Nano Letters* **19**, 1039 (2019), ISSN 1530-6984, 1530-6992.
- [25] I. Martin, G. Refael, and B. Halperin, *Physical Review X* **7**, 041008 (2017), ISSN 2160-3308.
- [26] L. Peralta Gavensky, G. Usaj, D. Feinberg, and C. A. Balseiro, *Physical Review B* **97**, 220505 (2018), ISSN 2469-9950, 2469-9969.
- [27] F. Harper, R. Roy, M. S. Rudner, and S. Sondhi, *Annual Review of Condensed Matter Physics* **11** (2020), ISSN

- 1947-5454, 1947-5462.
- [28] J. Clarke, A. N. Cleland, M. H. Devoret, D. Esteve, and J. M. Martinis, *Science* **239**, 992 (1988), ISSN 0036-8075, 1095-9203.
 - [29] P. Jarillo-Herrero, J. A. van Dam, and L. P. Kouwenhoven, *Nature* **439**, 953 (2006), ISSN 0028-0836, 1476-4687.
 - [30] P. W. Anderson and A. H. Dayem, *Physical Review Letters* **13**, 195 (1964), ISSN 0031-9007.
 - [31] C. D. English, D. R. Hamilton, C. Chialvo, I. C. Moraru, N. Mason, and D. J. Van Harlingen, *Physical Review B* **94**, 115435 (2016), ISSN 2469-9950, 2469-9969.
 - [32] G. Nanda, J. L. Aguilera-Servin, P. Rakyta, A. Kormányos, R. Kleiner, D. Koelle, K. Watanabe, T. Taniguchi, L. M. K. Vandersypen, and S. Goswami, *Nano Letters* **17**, 3396 (2017), ISSN 1530-6984, 1530-6992.

Supplemental Materials

S1. SAMPLE INFORMATION

The hexagonal boron nitride/ graphene heterostructure was assembled by the standard dry transfer stamping method from mechanically exfoliated flakes. The stack was then deposited on a silicon chip with a 280 nm oxide layer. The contacts were made of sputtered Molybdenum-Rhenium alloy (50-50 by weight), a type-II superconductor with a high critical temperature of 8 – 10 K. The junction has dimensions of $0.5 \times 3 \mu\text{m}$ and has been previously used as a reference device in Ref. 24. The MoRe contacts were connected to measurement lines through Cr/Au leads and bonding pads. By comparison to the simulations, we believe these leads and bonding pads act as the part of the environment which determines junction dynamics [28]. We model them as a resistor R_L in series with the capacitor C_0 .

S2. MEASUREMENT TECHNIQUES

While differential resistance maps are often measured using a lock-in amplifier, in this case hysteretic switching prevented us from using this technique. Instead, for each vertical line of the maps, an approximately 20 Hz triangle wave was applied and the resulting voltage profile was measured. 200 such measurements were then averaged to produce an $I - V$ curve and then numerically differentiated. These parameters allowed for fast measurements with reasonable averaging and minimal distortion of the applied wave by the low-temperature filters. We note that the exact extent of hysteresis is a function of the sweeping speed, with faster sweeping giving more pronounced hysteresis. This is particularly relevant when comparing to the numerical results, as the simulations used much shorter time evolutions thereby exaggerating the effects of the hysteresis.

S3. SIMULATIONS

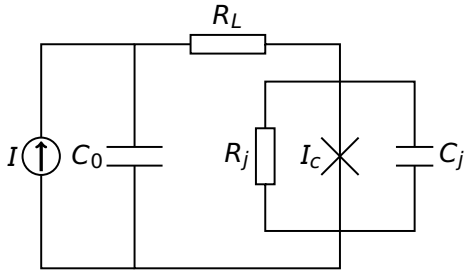


FIG. S1. Diagram of the circuit used to simulate the dynamics of the Josephson junction. In practice, C_j is negligible and is omitted from further consideration.

To simulate the behavior of a Josephson junction subject to microwave radiation, we use a modified RCSJ model as illustrated in Fig. S1 [29]. We start with a junction with critical current I_C , which is shunted by a resistor R_j and a capacitor C_j , where R_j represents the dissipation in the Josephson junction and C_j is the capacitance between the two superconducting leads. In the experiment, the Josephson junction is further connected to four $150 \mu\text{m} \times 100 \mu\text{m}$ bonding pads by Cr/Au leads. The capacitance of the bonding pads, C_0 , and the resistance of the leads, R_L , must be taken into account to properly simulate the junction dynamics. The four bonding pads are arranged such that the effective capacitance is equal to that of one bonding pad to the back gate, which would yield 1.8 pF for 280 nm thick SiO_2 . At room temperature, the capacitance between two bonding pads and bonding wires connected to the chip carrier by bonding wire was measured to be slightly higher, around 2.5pF, which was the value used in the simulations. In practice, similar maps have been simulated using a range of C_0 values.

The resistance of the evaporated Cr (5 nm)/Au (45 nm) film was measured to be 0.5 Ohm/ \square , from which we estimate that R_L is a few tens of Ohms for our typical devices. We use a reasonable value of $R_L = 50$ Ohms for our simulations in Figure 3 of the main text and in the simulations below. Finally, $R_j = 300$ Ohms is determined from the current corresponding to the center of the Shapiro plateaus in the Bessel function regime, $I_n = n\hbar\omega/R_j$. In accordance with the experiment, we assume that R_j does not depend on magnetic field. The same value of $R_j = 300$ Ohms is used to simulate all panels in Figure S2.

The microwave injection from the antenna can be modeled by a AC current, $I_{AC} = I_{RF} \sin \omega t$ where I_{RF} is the current amplitude and ω is the microwave frequency. Note that a significant amount of the applied power is dropped across the capacitors in our model. The thermal noise of the resistive components in the experiment generates a Gaussian current noise I_N whose variance is proportional to the temperature T . We find that for good agreement with the data, the noise amplitude has to be taken higher than expected for thermal noise. This is expected, for two reasons: first, in simulations I_N is applied to the outside of the junction circuit, where it would be partially filtered by C_0 and R_L before reaching the junction. Second, while each point on the map is measured for millions of cycles, we simulate it over just ~ 500 drive cycles, so using a higher level of noise may be expected. We therefore, treat I_N as a fitting parameter. In summary, the current source I contains three components, the bias current, I_{bias} , the microwave radiation current, I_{AC} and the thermal noise, I_N .

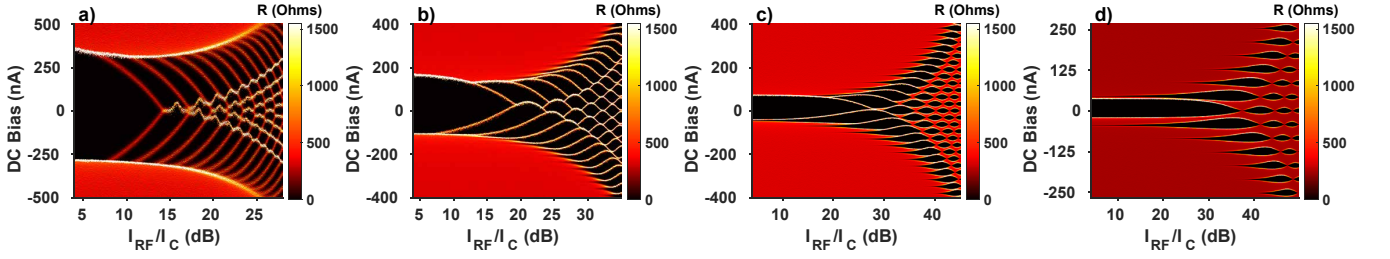


FIG. S2. Simulations of the differential resistance maps at 5 GHz for comparison to Figure 1a-d. The values of I_C used are, from left to right, 540, 200, 80 and 40 nA. Other parameters are kept the same as in Figure 3 of the main text: $C_0 = 2.5$ pF, $R_L = 50$ Ohms and $R_j = 300$ Ohms.

$$\begin{aligned}
 I &= I_{bias} + I_{RF} \sin \omega t + I_N(t) \\
 &= C_0 \frac{dV}{dt} + I_c \sin \phi + \frac{\hbar}{2eR_j} \frac{d\phi}{dt} + \frac{\hbar C_j}{2e} \frac{d^2\phi}{dt^2} \\
 V &= \frac{\hbar}{2e} \frac{d\phi}{dt} + R_L \left(I_c \sin \phi + \frac{\hbar}{2eR_j} \frac{d\phi}{dt} + \frac{\hbar C_j}{2e} \frac{d^2\phi}{dt^2} \right)
 \end{aligned} \quad (1)$$

The dynamics of the circuit in Fig. S1 is described by Eq. (1), where ϕ is the superconducting phase difference across the junction, V is the voltage across the capacitor C_0 and $I_N \propto \sqrt{T}$ is the standard deviation of the Gaussian noise. Solving this third order differential equation numerically gives $\phi(t)$, from which we can derive the DC voltage across the junction, $V_j = \left\langle \frac{\hbar}{2e} \frac{d\phi}{dt} \right\rangle$. Note that C_j is about 4 orders of magnitude smaller than C_0 for the device studied here. We numerically found that C_j can be neglected under this condition, simplifying Eq. (1) to a second order differential equation. The experimental curves strongly depend on the bias sweeping direction. To emulate the bias sweep, we use the steady solution of $\phi(t)$ at a given I_{bias} as the initial condition for solving the differential equation at the next value of bias, $I_{bias} + \delta I$, where δI is the incremental bias step.

Figure S2 shows simulated Shapiro maps at several values of the critical current, intended to be compared with the 5 GHz data of Figure 1. Remarkably, we are able to reproduce the four experimental maps in Figure 1a-d by changing only I_C , which is the only parameter we expect to be influenced by magnetic field. The values of $C_0 = 2.5$ pF, $R_L = 50$ Ohms, and $R_j = 300$ Ohms are kept the same in all panels.

Our model does not include heating from the RF drive, which has been recently identified to be an important effect [19]. We believe that such heating offers a natural explanation for the washed out features at higher RF power observed in the experimental data. Overall, the simple model describes the main features of our data sufficiently well.

S4. SIMULATION OF GATE VOLTAGE DEPENDENCE

Next, we reproduce the gate voltage dependence measured in Figure 4. Between the four maps, we adjusted the values of I_c and R_j , where the former can be obtained from the value of the switching current at zero RF power, and the latter could be roughly extracted from the positions of the Shapiro steps, $I_n = n\hbar\omega/R_j$. Additionally, the noise amplitude I_N was taken to be $\propto 1/\sqrt{R_j}$. This is consistent with the expectation that the noise in the junction is given by the thermal noise of R_j . While it may be expected that the noise processes in our driven system may be more complicated, the simulations capture the general trends observed in the data of Figure 4 of the main text.

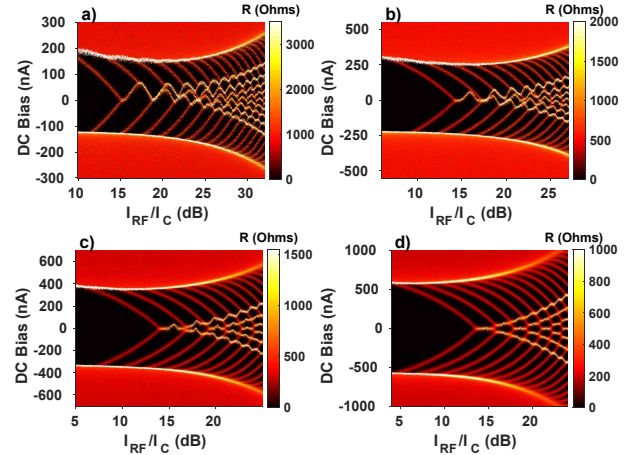


FIG. S3. Simulations of differential resistance maps corresponding to Figure 4 of the main text, measured at different gate voltages. We use the values of $R_j = 850, 500, 300, 180$ Ohms and $I_c = 350, 500, 600, 800$ nA in panels (a) to (d).

S5. CPR DEPENDENCE

Figure 1d of the main text shows strong fractional Shapiro steps [30], although there are no signs of fractional steps in the measurements with higher I_C . Our

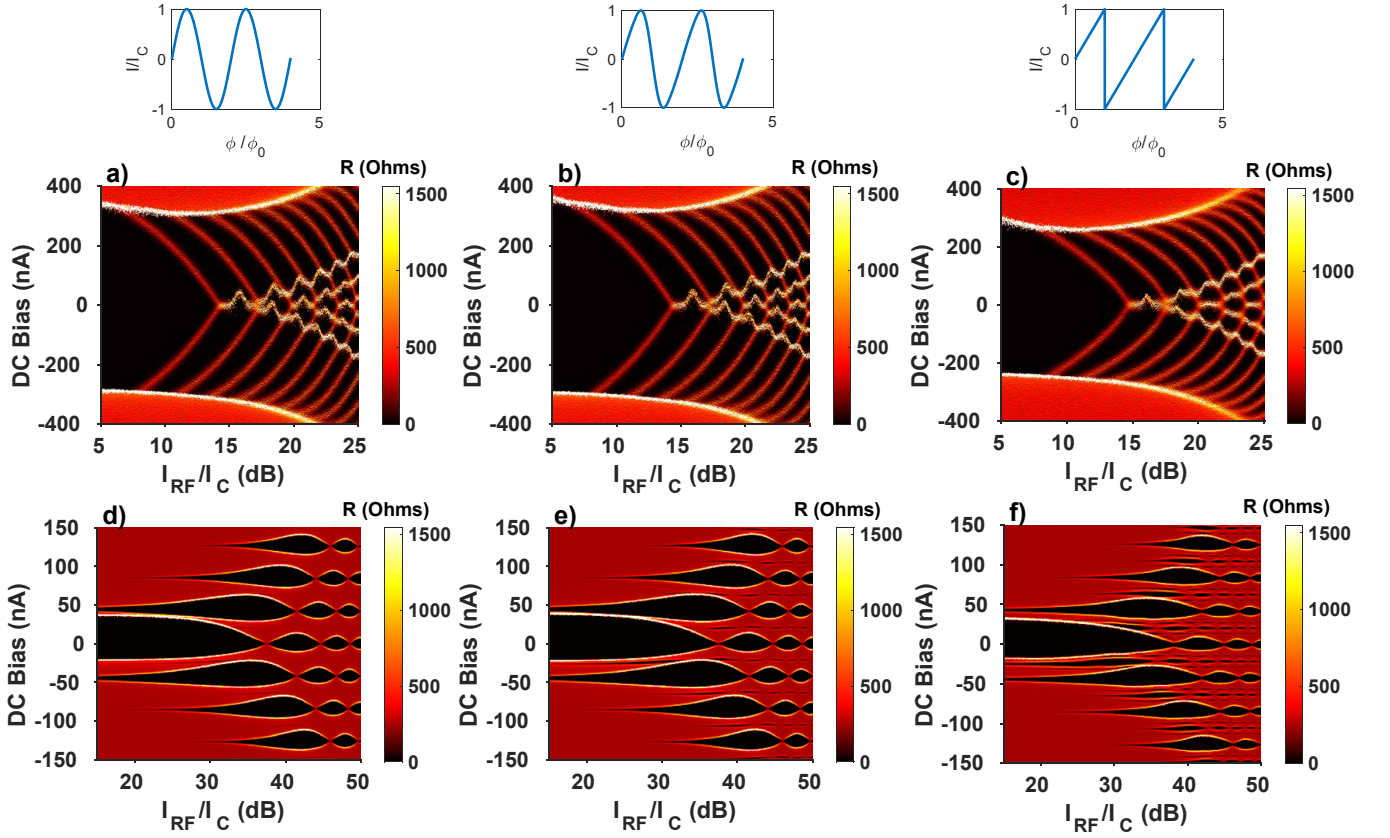


FIG. S4. Middle row: Simulations corresponding to Figures 1a and S2a with the skewness of the CPR increasing from left to right (the CPRs are shown in the insets). Even severe skewness does not give rise to fractional steps, although it does slightly alter the map in ways akin to changing parameters such as I_c and R_j . Bottom row: Simulations corresponding to Figures 1d and S2d with the same range of CPR skewness. In this regime, the CPR gives rise to enhanced fractional steps. Top row: CPRs corresponding to the figures below.

simulations are in an agreement with the experimental results, showing that a skewed CPR (current phase relationship) has minimal effect on a sample in the strongly hysteretic regime. Intuitively, we understand the hysteresis of the high I_c maps as arising from regions of overlapping stability of integer steps. Thus it may be expected that for such parameters the fractional steps are less stable compared to overlapping integer steps.

For comparison to the experiment, we took our simulation for Figures 1a and 1d and employed CPRs with varying degrees of skewness [31, 32]. In the top row, $I_c = 540$ nA, corresponding to Figures 1a and S2a; in the bottom row, $I_c = 40$ nA, corresponding to Figures 1d and S2d. The three columns correspond to: sinusoidal CPR (left), a slightly skewed CPR, $I(\phi) =$

$I_c[\sin(\phi) - 0.2\sin(2\phi) + 0.04\sin(3\phi)]$ (middle); and a maximally skewed sawtooth CPR (right). The insets in the top panels demonstrate the corresponding CPRs. For large I_c simulations, increasing the skewness of the CPR only slightly distorted the map, but did not give rise to any additional plateaus. For small I_c , increasing the skewness resulted in increasing fractional plateaus. Surprisingly, for small I_c even a perfectly sinusoidal CPR shows some half-quantized steps (Figure S4d). We attribute this behavior to the high frequency environment, which gives rise to some effective skewness. Comparing these simulations to the measured data, we find that the slightly skewed CPR appears to most accurately reproduce the strength of the fractional steps, as expected.